Available online at www.sciencedirect.com

ScienceDirect

Advances in Space Research 65 (2020) 1447–1465

ADVANCES IN SPACE RESEARCH (a COSPAR publication)

www.elsevier.com/locate/asr

Sentinel-1 interferometry with ionospheric correction from global and local TEC maps for land displacement detection in Taiwan

Wan-Ting Liao [a], Kuo-Hsin Tseng [a,b,*], I-Te Lee [c], Aive Liibusk [d], Jui-Chi Lee [e], Jann-Yenq Liu [a,f], Chung-Pai Chang [a], Yu-Ching Lin [g]

[a] Center for Space and Remote Sensing Research, National Central University, Taiwan
[b] Graduate Institute of Hydrological and Oceanic Sciences, National Central University, Taiwan
[c] Central Weather Bureau, Taiwan
[d] Department of Geomatics, Institute of Forestry and Rural Engineering, Estonian University of Life Sciences, Estonia
[e] Institute of Earth Sciences, Academia Sinica, Taiwan
[f] Graduate Institute of Space Science, National Central University, Taiwan
[g] Department of Environmental Information and Engineering, Chung Cheng Institute of Technology, National Defense University, Taiwan

Received 23 April 2019; received in revised form 4 November 2019; accepted 29 November 2019
Available online 10 December 2019

Abstract

Sentinel-1 satellite launched by the European Space Agency (ESA) offers an opportunity to apply the differential interferometric synthetic aperture radar (DInSAR) in 12-day revisit, a potential solution to effectively measure surface deformation. However, for areas affected by the Equatorial Ionization Anomaly (EIA) in a global ionosphere pattern, the total electron content (TEC) irregularity between snapshots may induce extra fringes and further mislead the unwrapping and displacement results. To test the necessity of ionospheric correction, we utilize global and regional ionospheric vertical TEC maps, namely the Global Ionosphere Map (GIM) released by the International GNSS Service and the Taiwan Regional Ionospheric Map (TRIM) provided by a local GNSS network, to compensate ionospheric phases in the interferograms.

Our experiments investigate 47 ascending image pairs in 2016 and 2017. Among them, two pairs of images whose differenced TEC (ΔTEC) stronger than 16.73 TEC unit in azimuthal gradient contain the clearest extra fringes. The results show that TRIM outperforms in reducing extra fringes caused by the ionospheric effect, with a root-mean-square error (RMSE) of the estimated satellite line-of-sight displacement reduced from 105.03 mm to 9.94 mm as compared against ground truth data. We conclude that TRIM TEC map is able to remove long-wavelength background of ionosphere-induced displacement when a differenced TEC gradient larger than an empirical threshold of 15 TECU.

Keywords: DInSAR; Equatorial ionization anomaly; Total electron content; Coseismic deformation

1. Introduction

Taiwan is located on the margins of two convergent plates: the Eurasian Plate and the Philippine Sea Plate. Owing to the enduring subduction and collision in the geological history, this interface exhibits high convergent rates (7–8 cm yr^{-1}) and frequent fault activities (Bos et al., 2003). Except for natural forcing, Taiwan also experiences surface deformation as a result of many anthropogenic impacts, such as land subsidence caused by over-pumping of groundwater to match the needs in agriculture and aquaculture usage (Hung et al., 2010; Tung & Hu, 2012).

* Corresponding author at: Center for Space and Remote Sensing Research, National Central University, Taiwan.
E-mail address: khtseng@csrsr.ncu.edu.tw (K.-H. Tseng).

https://doi.org/10.1016/j.asr.2019.11.041
0273-1177/

Although the subsidence rates in recent years have been decelerated thanks to several prevention policies, it is still a critical issue for residence and urban development in southwestern alluvial plain. Therefore, a systematic and effective way to monitor land deformation countrywide is urgently needed. One of the practical solutions is to use the Differential Synthetic Aperture Radar Interferometry (DInSAR) technology from spaceborne observations.

Several studies had demonstrated the efficiency and accuracy of land monitoring by using DInSAR approach (Pathier et al., 2003; Hsieh et al., 2011; Tung and Hu, 2012). However, in earlier years this technology had been limited to data availability, especially the high cost of images and processing complexity. Since the launch of Sentinel-1 by the European Space Agency (ESA) in 2014, many studies have investigated using satellite radar data for large-scale surface observation (González et al., 2015; Huang et al., 2016) in a regular manner. Its C-band SAR payload and precise orbit is suitable for observing short-term land deformation. Sentinel-1 following the open-data policy of the Copernicus Program starts a new era to provide wide swath and short revisit images globally at no cost to the end user. Taking these advantages, one can easily access time series images to generate interferograms over a large area for geodetic measurements.

However, the interferometric phase in each paired image not only contains actual land movements, but also experiences external errors for various reasons, such as orbit inaccuracy, topography, atmosphere (troposphere and ionosphere disturbances), and phase noises. These factors induce uncertainties between observations and actual land motions. Although the longer wavelength, for instance L-band (23.5 cm), encounters stronger ionospheric effect than C-band (5.6 cm) due to the inversely proportional relationship between dispersive phase and frequency under the same amount of electron content (Feng et al., 2017), it has been reported that C-band Sentinel-1 interferogram could be also affected by ionosphere in some cases (Gomba et al., 2017). Most of earlier studies in Taiwan often cropped a relatively small spatial window to city or county level (<50 km wide), allowing the ionospheric effect to be mitigated by some empirical methods. However, for a large coverage especially in latitudinal range, strong ionospheric anomaly would induce obvious fringes in the interferograms and deteriorate the displacement estimates. In addition, Taiwan is situated on the north edge of the Equatorial Ionization Anomaly (EIA) in a global ionospheric pattern. Diurnal ionization of the upper part of atmosphere due to solar radiation would induce variant strength of total electron content (TEC) (Tseng et al., 2010) and form a crest drifting around ±17° magnetic latitude. Hence, the unmodeled ionospheric variations between master and slave images are likely to induce extra fringes in the along-track (azimuth) direction.

To solve this issue, some research used the multi-frequency to quantify phase contribution from ionosphere. For example, the range split-spectrum method separates dispersive characteristic from other non-dispersive terms in an interferogram (Brcic et al, 2010; Rosen et al., 2010; Fattahi et al., 2017; Gomba et al, 2016, 2017). The azimuth pixel shifts method analyzes the misalignment of pixels in a sequence of acquisitions to derive ionospheric phase contribution (Mattar and Gray, 2002; Gilman et al., 2013; Zhu et al., 2016, 2017). However, the implementation of these strategies either relies on the coherent/incoherent cross correlation from multiple apertures and/or is sensitive to the correctness of unwrapped phase in the interferogram. In some extreme cases such as a spatial gap in the azimuth offset, these methods may not be properly carried out. Here, we seek for the observed ionospheric data recovered from a Global Navigation Satellite System (GNSS) network, to obtain the TEC during each Sentinel-1 snapshot and to assess its corresponding effect in the interferogram. This ground-based TEC map is presumably more complete in presentation of ionospheric patterns on different spatiotemporal scales. We first collect all Sentinel-1 single look complex (SLC) images in its ascending track covering Taiwan in 2016–2017, and then calculate their corresponding TEC differences from ionospheric maps. The reason we focus on ascending track is because of its local time (~6 pm) that is prone to be ionosphere-contaminated. A collection of descending passes (~6 am) over Taiwan in the same period is also analyzed (see Appendix A). However, the TEC difference between images are generally lower in the morning. For ascending tracks, two out of 47 pairs are detected to have prominent dense fringes, owing to a strong along-track TEC differences as compared with others (see later in Fig. 4). These two interferograms are compensated with ionosphere-derived phases, and then be unwrapped using the Statistical-Cost, Network-Flow Algorithm for Phase Unwrapping (SNAPHU) module (Chen and Zebker, 2002). Finally, the corrected line-of-sight (LOS) displacements are validated with land motions measured by GNSS continuous stations.

In the following sections, Section 2 introduces study area and our processing diagram for Sentinel-1 data. In Section 3, detailed data properties and methods are provided. In Section 4, comparisons of two selected cases before and after ionosphere compensation are conducted. An overall accuracy with or without ionosphere phase screen is provided. TEC difference and its potential threshold to influence interferograms is discussed in Section 5. Finally, some conclusions and limitations are summarized in Section 6.

2. Study area and workflow

Taiwan has experienced frequent land deformation due to its particular geological location. Strong earthquakes ($M_L > 5$) happen occasionally every few years. However, InSAR-derived surface deformations may be inaccurate without applying appropriate corrections, especially for the entire swath covering >100 km in azimuth. Two cases showing strong TEC effects in the interferogram as

mentioned before are fortuitously timestamped in the preseismic and coseismic period of an earthquake occurred on 6 February 2016 (M_L = 6.6; depth = 14.6 km; Epicenter = 120.54°E, 22.92°N) in Meinong District, Kaohsiung City, Taiwan. Many infrastructures were damaged during this event while 117 people were killed and more than 500 people were injured by collapsed buildings. This was one of the most disastrous earthquakes in Taiwan since the Chi-Chi earthquake (M_L = 7.3; depth = 33 km) struck in 1999.

The epicenter of Meinong earthquake is depicted as yellow star in Fig. 1, where a dense GNSS network used for retrieving ionospheric TEC in the Taiwan Regional Ionospheric Map (TRIM) are denoted as blue dots. Another GNSS network used for validating DInSAR surface deformation are marked as red dots in Fig. 1. The inset map indicates the full coverage of TRIM processed from those blue dots in the main figure. Black line represents Sentinel-1 ground track section for images in this study. The imaging frame and the corresponding ionospheric penetration window at 350 km are denoted as red and blue box, respectively.

The workflow is summarized in Fig. 2, in which left part (green) explains DInSAR process by using some default steps in the Generic Mapping Tool SAR (GMTSAR) open-source software (Sandwell et al., 2011, 2016; Xu et al, 2017), and right part (red) explains ionospheric phase correction from referenced TEC maps. Finally, the excessive ionospheric phase is removed from the interferogram and proceed with unwrapping solution to obtain the final displacement.

3. Data and processing method

3.1. Sentinel-1 data

Sentinel-1A is the first flight unit of its twin-satellite architecture, followed by the unit B launched two years

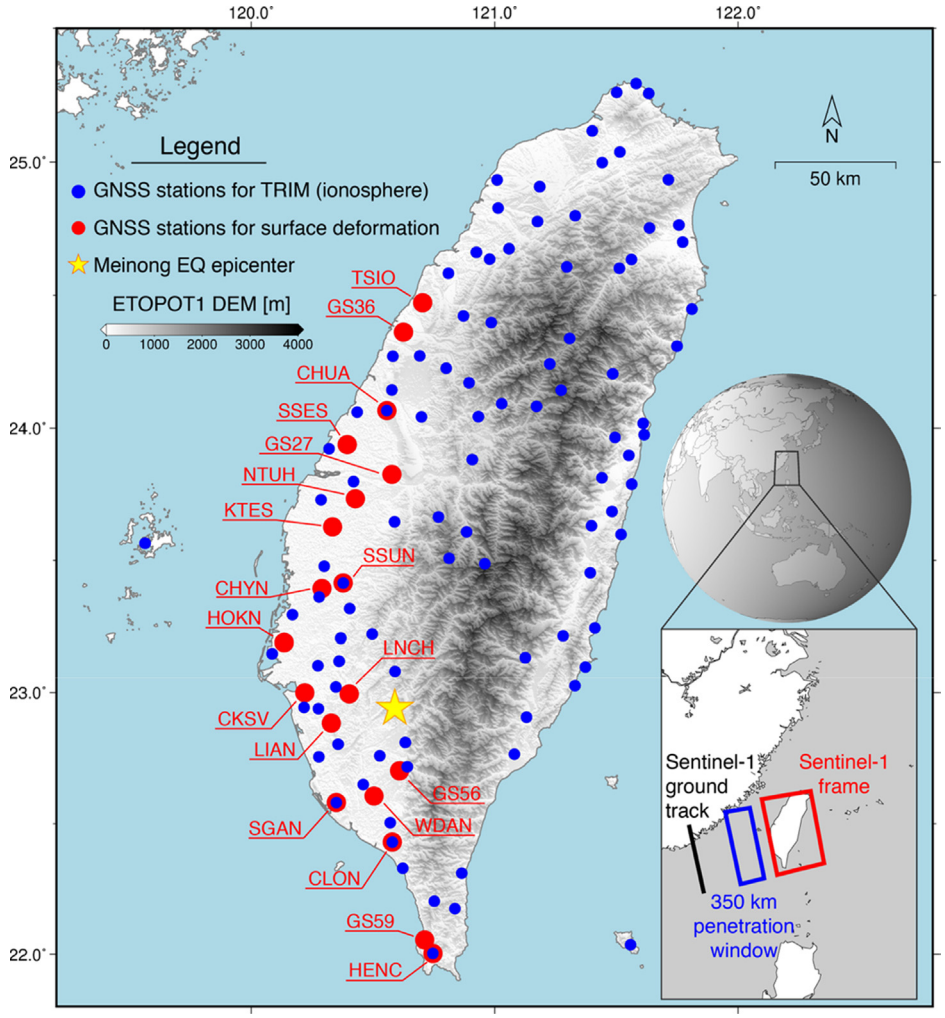

Fig. 1. (Main) Locations of a GNSS network for retrieving TRIM ionospheric TEC (blue dots) and another GNSS network for validating surface deformation (red dots). Meinong earthquake epicenter is denoted as yellow star. (Inset) Map area indicates the coverage of TRIM. Black line is Sentinel-1 ground track section for images in this study. The imaging frame and the corresponding penetration window at 350 km are denoted as red and blue boxes, respectively. (For interpretation of the references to color in this figure legend, the reader is referred to the web version of this article.)

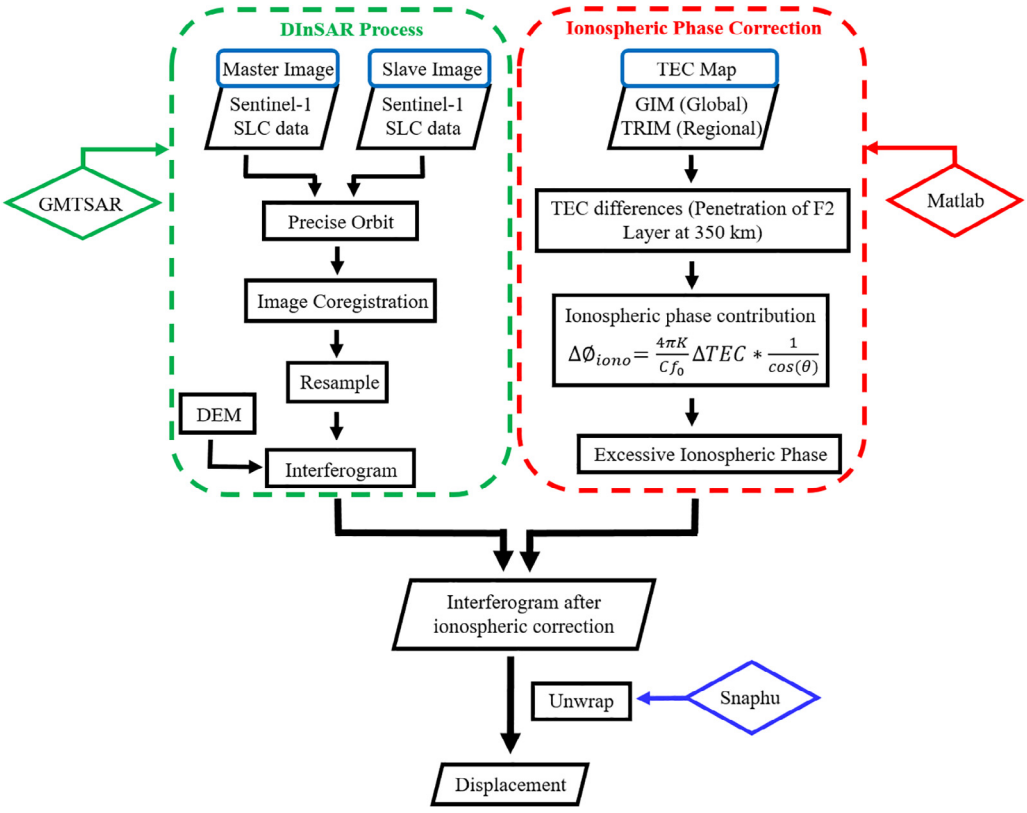

Fig. 2. Flow chart of DInSAR composition and ionosphere correction by GMTSAR and MATLAB, respectively.

later in 2016. It is equipped with a C-band (5.6 cm) SAR operated in Terrain Observation with Progressive Scans SAR (TOPSAR) mode. TOPSAR is known to improve the signal-to-noise ratio among sub-swaths from conventional ScanSAR mode, and to provide a wide coverage of surface observation. The Interferometric Wide (IW) swath mode with 5 × 20 m spatial resolution is the main acquisition mode in Taiwan, where each swath covers an area of 250 km in range and 170 km in azimuth directions. Another advantage of Sentinel-1 is the well-maintained orbit that shortens the baseline between master and slave images, which efficiently decreases spatial baseline decorrelation. Short revisit time in every 12 days provides near real-time information for monitoring ground surfaces. For the timespan in 2016–2017, we download 51 Sentinel-1A single-look-complex (SLC) images in the ascending track #69, including the south frame #69 and the north frame #74, from ESA's Copernicus Open Access Hub.

3.2. GIM and TRIM TEC maps

Two types of TEC maps are used in this study. Global Ionosphere Map (GIM) generated every 2 h is released by the Center for Orbit Determination in Europe (CODE), using TEC data from about 200 GPS/GLONASS sites involved in the International GNSS Service (IGS) and other institutions (Jee et al., 2010). TEC value is calculated from GNSS signal delay caused by the ionosphere, and converted into electrons density. This TEC value in path direction is further transformed from the slant TEC (STEC) to the vertical TEC (VTEC) at the pierce point by using a mapping function. After that, spherical harmonics interpolation (Eq. (1)) (Schaer et al., 1995; Zhang and Zhao, 2019) is applied to these scattered measurements to produce a gridded TEC map with a spatial resolution in 5° and 2.5° for longitude and latitude, respectively (Table 1). Spherical harmonic expansion is one of the mathematical function-based models to avoid unreasonable extremes in VTEC estimates in regions where the point measurements are sparse (Schaer et al., 1998)

$$VTEC(\phi,\lambda) = \sum_{n=0}^{n_{max}} \sum_{m=0}^{n} \tilde{P}_n^m(\sin\phi)\left(C_n^m \cos(m\lambda) + D_n^m \sin(m\lambda)\right) \quad (1)$$

where ϕ is the geocentric latitude and λ is the sun-fixed longitude for the penetration point in a sun-fixed geomagnetism coordinate system, $\tilde{P}_n^m$ is the normalized associated Legendre polynomials with degree n and order m, C_n^m and D_n^m are the unknown coefficients of the spherical harmonics functions to be fitted. n_{max} is the maximum highest spherical harmonic degree depending on the designated spatial resolution.

Taiwan Regional Ionospheric Map (TRIM) was developed by the Ionospheric Radio Science Laboratory of National Central University, and it is now produced and published in real time by the Central Weather Bureau

Table 1
Characteristics of GIM and TRIM ionospheric map.

Ionosphere model	GIM	TRIM
Spatial coverage	180°W–180°E 87.5°S–87.5°N	115°E–127°E 17°N–32°N
Spatial resolution in longitude/latitude	5°/2.5°	0.5°/0.5°
Temporal resolution	2 h	5 or 20 min
Number of stations around Taiwan	3	100

(CWB) of Taiwan. It uses a local GNSS network mainly operated by CWB to monitor TEC variation in the visible sky. TRIM utilizes nearly 100 receiving stations in Taiwan, providing every 5- or 20-min update of temporal data with a spatial resolution at 0.5° in both longitude and latitude. The spatial coverage of TRIM ranges 115–127° in longitude and 17–32° in latitude. TRIM is also produced by the same methods as GIM that calculates GNSS signal delay caused from the ionosphere and converted into electrons density. Fig. 3 is a demonstration of GIM (panel *a*) and TRIM (panel *c*) with their full spatial coverage at 10:00 UTC on 14 February 2016. The color bar in each figure is TECU, a typical unit to describe electron density that equals to 10^{16} elections per unit square meter. As seen in the blow-up view of GIM (panel *b*) in the same area with TRIM, GIM is smoother in presentation of TEC structures.

3.3. GNSS land deformation

As mentioned before, Taiwan is located in a tectonically active region so that GNSS is widely used for monitoring displacements caused by earthquakes and plate motions. GNSS measurement in this study thus provides a reference to complement with and to validate InSAR results. A different network than the one mentioned in previous section (with only a few collocations) is operated primarily by the GPS LAB of Institute of Earth Sciences (IES), Academia Sinica, Taiwan (Fig. 1, red dots) (http://gps.earth.sinica.edu.tw). We chose 19 stations along the west plain for validating DInSAR displacement.

Due to the varying environmental conditions, GNSS daily solution contains high frequency oscillations. To reduce these noises without appropriate physical meanings, GNSS daily measurements are normally modeled in three directions with annual, semi-annual signals and postseismic signals, which can be presented by the following equation:

$$y(t) = a + bt_i + c\sin(2\pi t_i) + d\cos(2\pi t_i) + e\sin(4\pi t_i) + f\cos(4\pi t_i) + \sum_{i=1}^{N_h} gf\left(\frac{t-t_i^h}{t_c}\right)H\left(t-t_i^h\right) + \varepsilon \quad (2)$$

where t_i is the time epoch, H is the step function and f is the postseismic exponential decay (Hsu, 2006; Helmstetter & Shaw, 2009). The first two terms are the static offset a and the linear rate b. Coefficients c and d represent the amplitude of annual signal while e and f are those of semi-annual signals. g is the amplitude of postseismic displacement modelled by a step function and exponential decay with the relaxation time of t_c. The last term ε is the residuals.

Since GNSS data shows three-dimensional displacement in east (E), north (N), and up (U) directions, all these components are mapped to the satellite light-of-sight (LOS) direction to compare with DInSAR results. GNSS time series can be projected into LOS displacement by the following equation:

$$GPS_{LOS} = \begin{bmatrix}\cos\theta & \sin\alpha\sin\theta & -\cos\alpha sin\theta\end{bmatrix}\begin{bmatrix}GPS_U\\GPS_N\\GPS_E\end{bmatrix} \quad (3)$$

where θ is the incidence angle and α is the azimuth angle of the satellite.

To further detail the validation procedure, a spatial window of 0.01° × 0.01° (around 1 × 1 km) centered at each GNSS station is set to calculate an average of DInSAR displacement. This value indicates a smoothed DInSAR displacement near each GNSS station between master and slave time. Because DInSAR depicts the relative displacement between two dates, we use the master date as a benchmark to see if the displacement after correction agrees with GNSS time series.

3.4. Ionospheric phase in the interferogram

The causes of interferometric phase change include dispersive and non-dispersive mechanisms. Non-dispersive terms are the differential path delay associated with ground movement between two images, the topographic path delay, and the differential tropospheric path delay (Fattahi et al., 2017). The dispersive nature of radar waves in the ionosphere induces a frequency-dependent pattern of phase advances. For longer microwave wavelength or low frequency, e.g., the Phased Array type L-band Synthetic Aperture Radar (PALSAR) onboard the Advanced Land Observing Satellite (ALOS) of The Japan Aerospace Exploration Agency (JAXA), wave propagation encounters more phase advance effects in the media. For shorter wavelength (i.e., C-band, Sentinel-1A), the signal experiences relatively fewer disturbances (Meyer et al., 2006; Jung et al., 2013; Gomba et al., 2017).

Moreover, propagation of microwave signal through ionosphere causes phase advance of the carrier, Faraday rotation, defocusing of SAR image, and extra shift between SAR images in the azimuth direction (Fattahi et al., 2017). Phase advance is the main effect considered in this study, which can be calculated by an integration of electrons density along the two-way wave path (Gomba et al., 2016), such as:

$$\varnothing_{iono}(f) = 2 * \frac{2\pi K}{Cf_0} * \int n_e(z)dz = \frac{4\pi K}{Cf_0}STEC \quad (4)$$

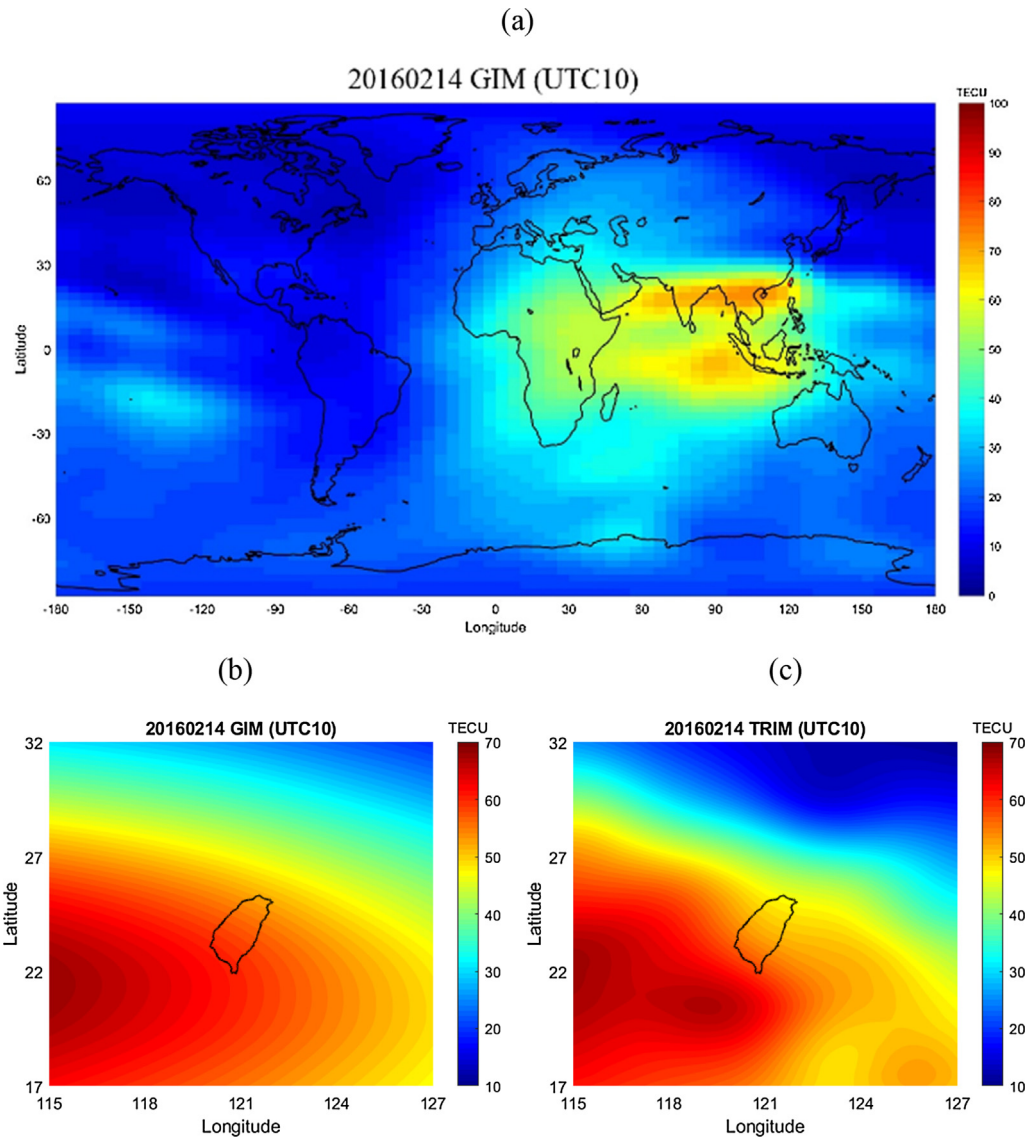

Fig. 3. An example of (a) full coverage of Global ionosphere map (GIM), (b) regional zoom-in of GIM, and (c) full coverage of Taiwan Regional Ionosphere Map (TRIM) on 14 February 2016 at 10:00 UTC. Color-code is the value in TECU.

where C is the speed of light in vacuum, f_0 is the carrier frequency of Sentinel-1A equal to 5.4×10^9 Hz, K is a constant equal to 40.28 m^3/s^2, n_e is the electrons density, and slant TEC $= \int n_e(z)dz$.

Next, phase advance in the interferogram between master and slave images can be modeled as:

$$\Delta\varnothing_{iono} = \frac{4\pi K}{Cf_0}\Delta TEC * \frac{1}{cos(\theta)} \quad (5)$$

where ΔTEC hereafter represents VTEC (simplified from STEC in Eq. 4) difference between master and slave images in vertical direction. θ is the incidence angle of satellite, which varies from 29° to 46° in west to east for Sentinel-1 in our study area.

The spatial distribution of ionosphere is usually assumed as a shell layer, where the height maxima of F2 layer (HmF2) indicates the height of ionosphere electron density reaching its maximum in vertical structure. Spatiotemporally varying HmF2 is available from a few sophisticated products, such as the International Reference Ionosphere (IRI) model. Around Taiwan area, HmF2 reaches around 350 km above the Earth's surface. Therefore, a constant value at 350 km is chosen as the penetration window of SAR signals (inset of Fig. 1, blue box). It presents the strongest electrons density to influence the propagation of microwave.

In the ascending track of Sentinel-1A, the right-looking imaging geometry means that the ground track passes through west of Taiwan (inset of Fig. 1, black line). Hence, the penetration window of microwave through HmF2 is projected in between ground track and the imaging window along the LOS direction. Since Eq. (4) also considers the

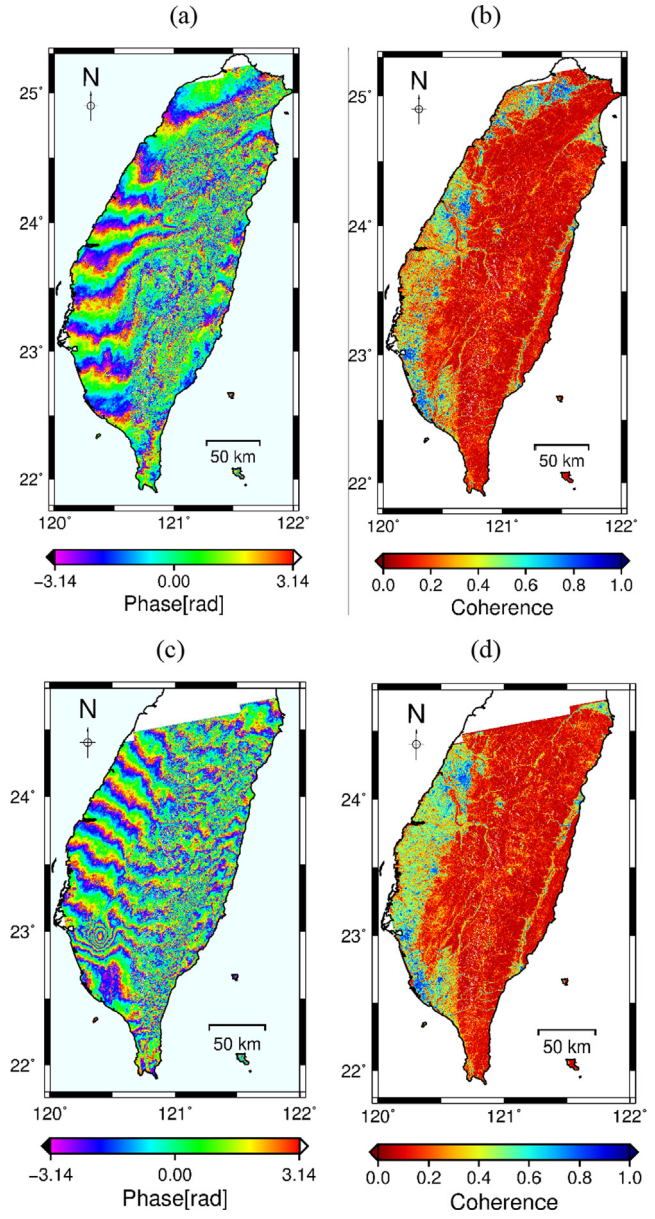

Fig. 4. Original interferogram and coherence map in Case 1 (panel *a* and *b*) and 2 (panel *c* and *d*). In coherence map, warm to cold colors indicate coherence being low to high.

incidence angle of satellite (θ), slant direction is calculated for each pixel. After modeling GIM/TRIM ionospheric phase by Eq. (4), the quantity is compensated in the original interferogram produced by GMTSAR.

4. Results and validation

Two cases with clear ionospheric contamination are firstly shown here to demonstrate the efficacy of ionosphere phase screening. Case 1 is a set of preseismic images before the Meinong earthquake happened on 6 February 2016. The master and slave images were taken on January 9, 2016 and February 2, 2016, respectively. Case 2 contains the coseismic pattern of Meinong earthquake, for which the master and slave images are from February 2, 2016 and February 14, 2016, respectively (Table 2).

As displayed in Fig. 4, both original interferograms contain ~10 extra fringes in the along-track direction, as shown in panel *a* (Case 1) and *c* (Case 2). Such a strong phase gradient is not associated with other known error sources. For example, an orbit error of 5 cm only induces 0.2–0.5 rad of phase error in each 50 km on the ground from a simulation of C-band SAR (Reigber et al., 1997). Meanwhile, the additional path delay caused by troposphere would present with local weather and terrain patterns, which is significantly different from orbital or ionospheric artifacts (Gomba et al., 2017; Yu et al., 2018). Flat terrain along the western alluvial plains (Fig. 1) is less likely to induce topographic errors. Therefore, the primary reason of this phase gradient is attributed to the different strength of TEC. Right column of Fig. 1 displays coherence map associated with land types and their temporal variabilities. Mountain areas with forest cover appear much lower coherence in response to C-band radar. We will mask out lower coherence (<0.4) pixels in the following analysis for better visualization.

4.1. Case 1: Preseismic motion before the Meinong earthquake

In the original interferogram of Case 1, some extra fringes induced by ionosphere exist in the west of Taiwan (Fig. 4a). Following the flow chart specified in Fig. 2, we first crop a spatial window to obtain the TEC difference at 350 km in the penetration window (Table 3, middle column), and then simulate its ionospheric phase contribution in the wrapped form (Table 3, right column). A differenced TEC (ΔTEC) is calculated between master and slave timings in the blue box of Fig. 1 at the passing time of 10:00 UTC (18:00 Local Time). As seen in the left column (ΔTEC near Taiwan) and middle column of Table 3, TRIM based on regional data presents more details in ionospheric pattern than GIM, especially in the meridional variation. In ΔTEC map between master and slave images, TRIM shows a clearer difference from north to south than GIM and produces more fringes in the next step. As compared with the original interferogram, ionospheric phase calculated by Eq. (4) for TRIM has a similar pattern of parallel fringes.

Table 4 shows the interferogram before and after ionospheric correction by two models. It can be seen that GIM providing inaccurate ionospheric phases leaves obvious extra fringes after correction. Instead, TRIM sufficiently removes the pattern imposed by ionosphere lying along the latitudinal direction. Furthermore, unwrapped displacements before and after ionospheric correction are demonstrated in the second row of Table 4. Here, a reference point for unwrapping is tied to SSES in Fig. 1, a station near the center of this network. Without appropriate correction, accumulative phase in central Taiwan contains incorrect N–S displacement owing to the ionospheric shift in the wrapped phases. After phase modification by TRIM,

Table 2
Images used in Case 1 and 2.

	Master image	Slave image
Case 1: Preseismic motion before the Meinong earthquake	2016/01/09	2016/02/02
Case 2: Coseismic motion across the Meinong earthquake	2016/02/02	2016/02/14

Table 3
Differenced TEC (ΔTEC) between master and slave images and phase contribution for Case 1.

M:2016/01/09 S:2016/02/02	ΔTEC around Taiwan	ΔTEC in penetration window at 350 km	Ionospheric phase
GIM	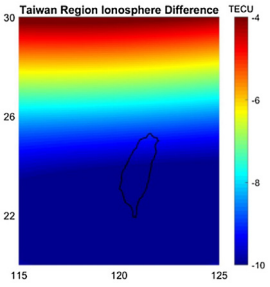	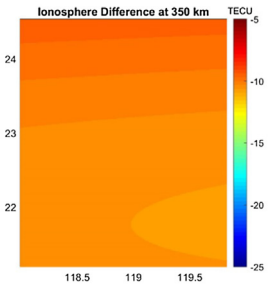	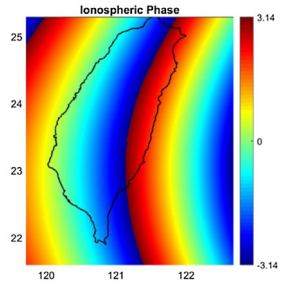
TRIM	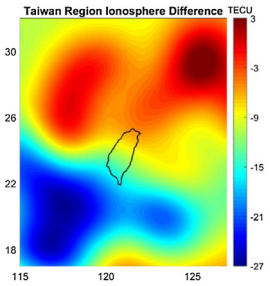	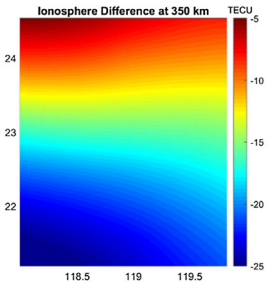	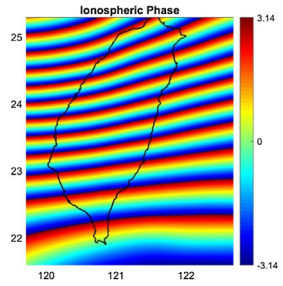

surface deformation becomes reasonable and smooth with fair extreme values. However, sparse coverage in the central ridge is still an inevitable problem due to dense vegetation and forest canopy, where the coherence in this area is relatively low (Fig. 4b). In order to check the improvement of correction over the unprocessed version, GNSS data will be used for validation in Section 5.

4.2. Case 2: Coseismic motion across the Meinong earthquake

As a strong coseismic movement caused by Meinong earthquake spreading some 50 km west to the epicenter, there are obvious concentric rings overlapped with several error fringes caused by ionosphere in the original interferogram (Fig. 4c). Following the same processing workflow, ΔTEC and the estimated phase contribution are shown in Table 5. Similar to the previous case, TRIM provides much more detailed information about ionospheric contamination than GIM in the penetration window. As each fringe of C-band Sentinel-1A corresponds to 2π ($-\pi$ to π) or 2.8 cm displacement along the LOS direction, a total of >12 fringes appearing in the lower right panel of Table 5 is equivalent to 33.6 cm of accumulated displacement in azimuth direction. In Table 6, it shows that after ionospheric correction by TRIM, the spatial pattern of paralleled fringes is removed while the co-seismic deformation caused by Meinong earthquake is well preserved. Displacement of coseismic deformation is estimated to be around 10 cm in LOS direction. The value is consistent with an extensive survey of 2016 Meinong earthquake conducted by Rau et al. (2017). This report also used Sentinel-1A ascending mode data in a smaller range window to calculate LOS deformation near the epicenter. It means that the deformation signal will not be interrupted by this correction method. Similar to the previous case, the displacement estimated by TRIM-corrected interferogram performs better than the conventional workflow, or by GIM-corrected one.

4.3. Validation with ground truth

A comparison between DInSAR displacement and GNSS ground measurement is displayed in Fig. 5, in which the performance of TRIM and GIM correction over 6

Table 4
Displacement before and after correction by TRIM and GIM, respectively, in Case 1.

	Before Correction	After Correction (TRIM)	After Correction (GIM)
Wrapped Interferogram	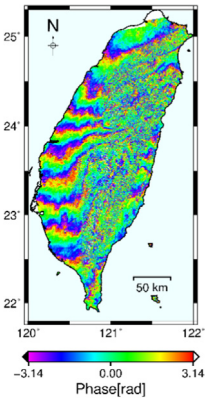	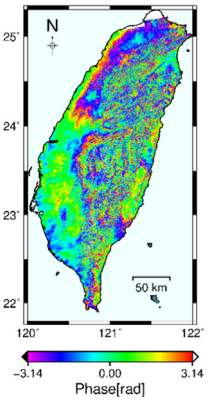	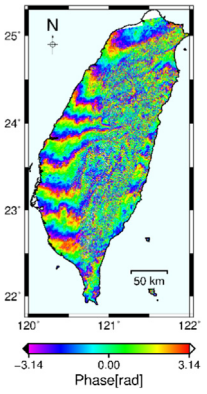
Displacement	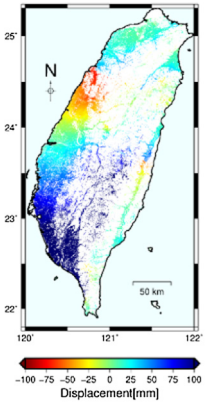	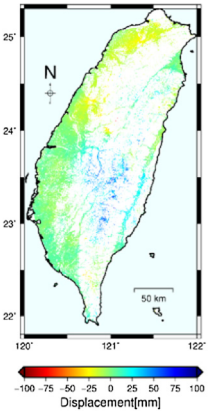	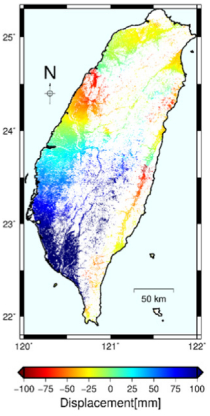

stations (mostly located in different latitudes) is visualized in a time series manner. Most of TRIM-corrected displacements (red triangles) are more consistent with GNSS time series (black line and dots) than the uncorrected version (blue dots). Actually, in these 19 stations dataset, a majority of DInSAR points have moved closer to the fitted GNSS time series (black line) after correction by TRIM. In contrast, using GIM (green circles) for ionospheric correction is not as workable in reducing extra fringes in the interferogram, where the displacement interpreted from green circles is still misleading. The coseismic displacement estimated by the split-spectrum (Gomba et al., 2016) and a filtering method (Fattahi et al., 2017) is also marked in each figure (blue triangles) for a comparison with the result in Gomba et al. (2017). It is calculated by a newly developed module (*estimate_ionospheric_phase*) implemented in GMTSAR v5.7. The result can be found in Fig. B1 in Appendix B.

It is noted that at GS27, the closest station to the reference point (SSES) for all methods, either TRIM or split-spectrum still exhibit an error of 15–18 mm in coseismic displacement. It indicates that the displacement after ionospheric correction may still contains errors from other sources. One may seek for ground controls such as leveling and GNSS co-kriging scheme (Huang et al., 2017) for refined solutions.

5. Discussions

5.1. Accuracy after ionosphere compensation

To quantify the accuracy before and after correction, a root-mean-square error (RMSE) is calculated between DInSAR and GNSS displacements for two kinds of correction method. RMSE can be computed by the following equation:

$$RMSE = \sqrt{\frac{\sum_{i}^{N}(X_{DInSAR,i} - X_{GNSS,i})^2}{N-1}} \quad (6)$$

where i means each of 19 station, X_{DInSAR} is DInSAR displacement estimated by an average from a buffer of 1 km around GNSS station, X_{GPS} is GNSS displacement between two dates, and N is the number of stations.

As listed in Table 7, RMSE in Case 1 is reduced from 83.77 mm (before correction) to 6.60 mm among all 19

Table 5
Differenced TEC (ΔTEC) between master and slave images and phase contribution for Case 2.

M:2016/02/02 S:2016/02/14	ΔTEC around Taiwan	ΔTEC in penetration window at 350 km	Ionospheric phase
GIM	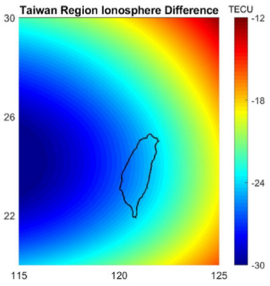	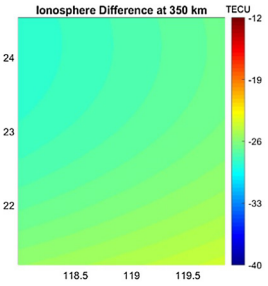	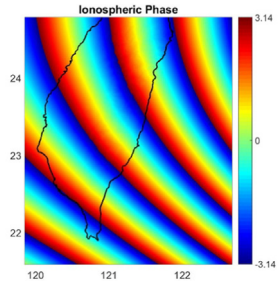
TRIM	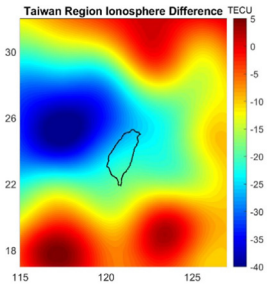	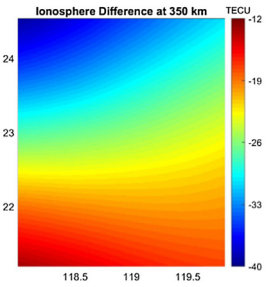	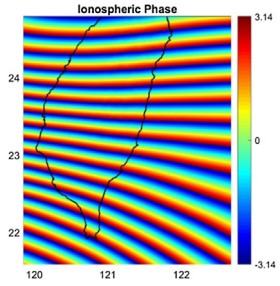

stations after ionospheric correction by TRIM. For Case 2, RMSE is reduced from 125.12 mm to 12.63 mm. Here, the RMSE of Case 2 using split-spectrum method as solved by GMTSAR is 19.86 mm (not shown in this table), at a similar level as TRIM's performance. For a combination of two, TRIM's RMSE is reduced from 105.03 mm to 9.94 mm. It illustrates that ionospheric phase compensation assisted by a TEC map is a feasible method to improve accuracy. However, GIM seems to be unable to provide sufficient information for phase correction. The RMSE down to 103.33 mm performs marginally better than the original interferogram without phase patches. The results are also presented in a scatter plot (Fig. 6) to show the performance before and after corrections from two maps. As moving toward to the 1:1 line (black line), TRIM-corrected points (red dots) including both cases display a smaller range of spread than GIM-corrected ones (green dots) as compared against in situ data.

5.2. Comparison between GIM and TRIM

Comparing two types of TEC maps, both products present electrons density inverted from the delay of GNSS signal while penetrating through the ionosphere layer. However, because TEC exhibits a few tens to hundreds kilometer of spatial wavelength, insufficient density of ground stations would not be able to capture the detail anomaly. GIM is a global TEC map with far fewer local stations, in which the nominal data source only includes 3 receiving stations around Taiwan. In contrast, TRIM consists of their own network with around 100 receiving stations in the main and outlying islands. In GIM, the global raster data include spherical harmonic interpolation on a regional scale, where the difference between real TEC and GIM could reach ~10 TECU. This difference is too large to show the detailed pattern for ionospheric correction. Therefore, TRIM is more suitable over this area to serve as supplemental data for radar observation.

5.3. Effect of TEC gradient

In a total of 47 ascending pairs examined in 2016 and 2017 (Appendix A), not every interferograms are sensitive to ionospheric activities. It depends on the strength of TEC and its spatial gradient. Thus, TEC difference between master and slave images in the penetration window at 350 km is important. One major finding in this research is that the N–S difference in the penetration window dominates extra fringes and misleads the original signal. As revealed in Table 8, a strong gradient of TEC difference could induce more fringes than a gradual gradient. In this case, it is more likely to influence interferograms as demonstrated in Case1 and 2 (an extra test of strong azimuth ΔTEC crossing the coseismic period but with a long temporal baseline (>1 month) is given in Fig. B2, Appendix **B**). However, for the rest cases with fewer N–S TEC difference, the effect on the interferogram is not that obvious, regardless how strong the mean TEC difference between images is (listed in Appendix A). In consequence, the effectiveness of TRIM-corrected interferogram also becomes

Table 6
Displacement of before correction and after correction by TRIM and GIM, respectively, in Case 2.

	Before Correction	After Correction (TRIM)	After Correction(GIM)
Wrapped Interferogram	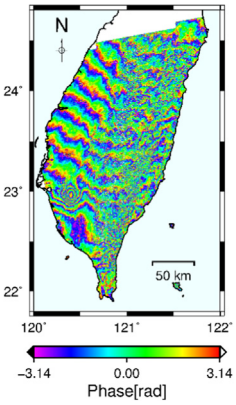	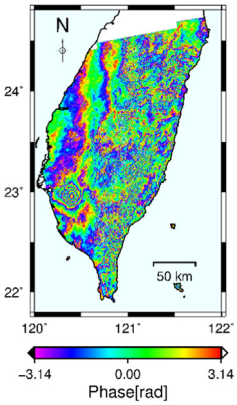	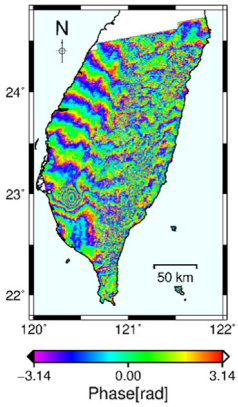
Displacement	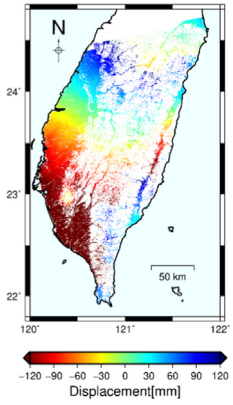	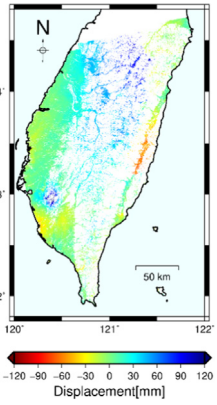	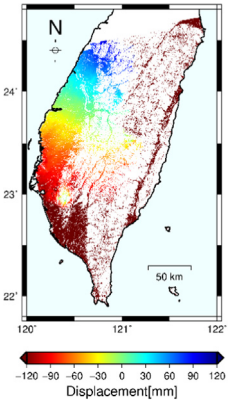

less prominent. Table 9 displays four more cases whose N–S TEC difference is lower than a threshold of ΔTEC (~15 TECU) demonstrated above. As seen in the decreasing order of Table 9, the zonal pattern of fringes becomes less noticeable (left column) and the removal of phases from TRIM only marginally modifies the spatial pattern of interferogram (right column). However, we also observe that the number of fringes is not proportional to ΔTEC in the cases of smaller ΔTEC gradient. Since the accuracy of TRIM TEC map at 2–3 TECU level will be worse through error propagation while generating a differenced map, and combined with other noises neglected in this study, it should be emphasized that the threshold (15 TECU) is an empirical number specifically for TRIM map under its unique spatiotemporal resolution and observational accuracy. The lower of ΔTEC estimated by TRIM, the less reliability of the excessive phase it can simulate.

5.4. Limitation of spatiotemporal resolution of TEC maps

Although the TEC map provided by CWB is interpolated from scattered points collected in a relative short epoch (5 min), the accuracy may still be insufficient to represent the instant (10–20 sec) acquisition time of SAR. To examine the possible uncertainty induced by the limitation of ground-based measurements, a few TEC maps in the epochs before and after the nominal satellite passing time of Case 1 are investigated to check whether the westward migration of EIA crest during a 5-minute interval (or approx. 125 km in equivalent) would be an issue. Three TEC maps before and after the central TEC map are applied in the same workflow and to compare the corrected LOS displacement with ground truth. Table 10 shows that the accuracy changes much while using neighboring TEC maps before or after the nominal SAR imaging time, especially during the increasing phase of EIA from its quiet hours (former periods). It indicates that the temporal resolution might be sensitive to this scale of spatial resolution.

It is also inferred that within this 5 min, high order ionospheric heterogeneities are not captured in the scattered measurement and/or be smoothed out in the following spherical harmonics interpolation. However, as long as the zonal structure of long-wavelength TEC background stays for a few minutes, the TEC gradient would pertain

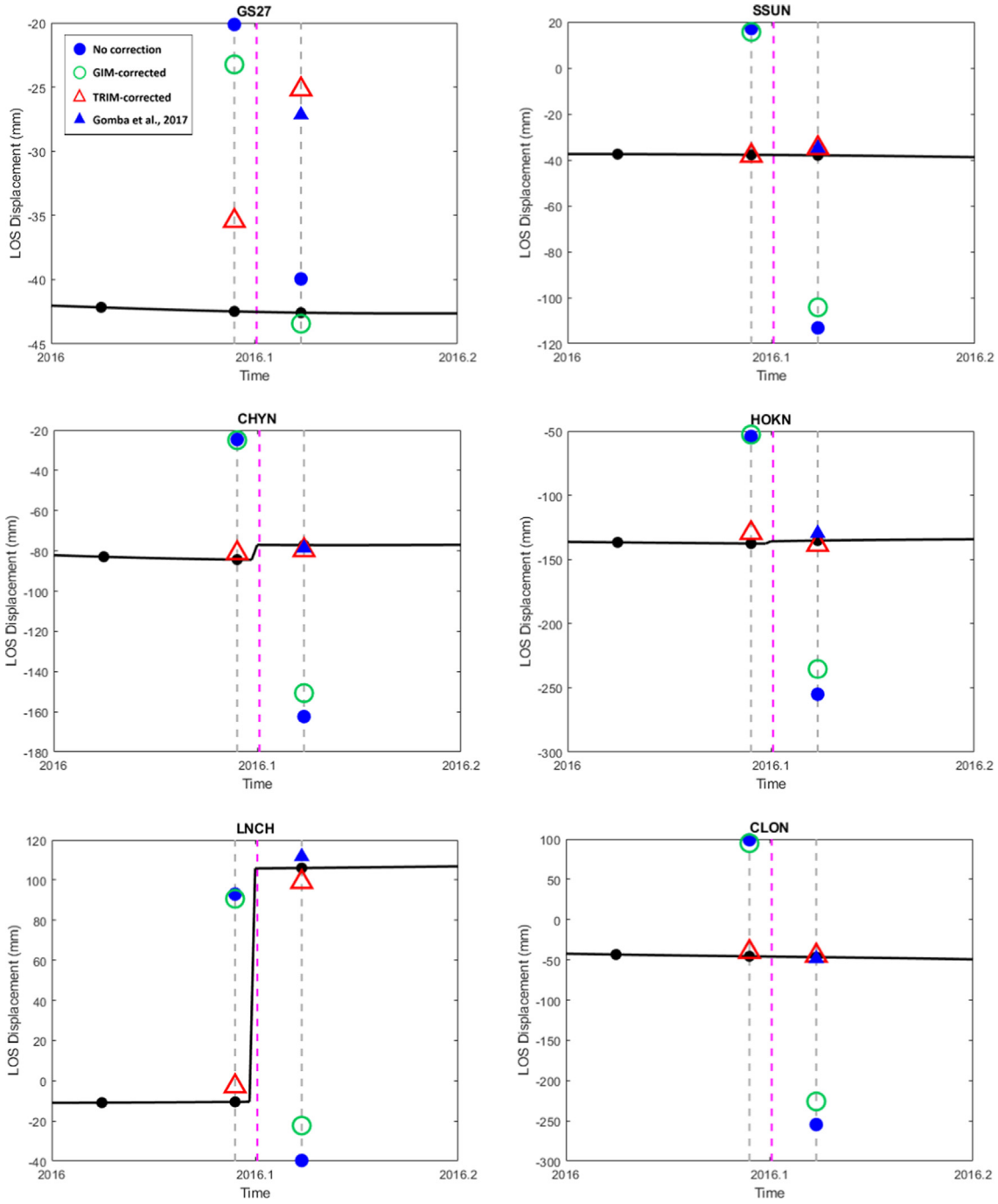

Fig. 5. Six examples of displacement estimated by GNSS and InSAR from north to south in the west plain. In each panel, black line indicates the modeled GNSS time series, black dots are the corresponding GNSS position on 9 January, 2 February, and 14 February, and blue dot is the relative displacement before correction in slave time. Red triangle, green circle, and blue triangle are the relative displacement from TRIM, GIM, and Gomba et al. (2017) corrections in slave time, respectively. Magenta dash line indicates the timing of Meinong earthquake. Gray dash line indicates the same day. (For interpretation of the references to color in this figure legend, the reader is referred to the web version of this article.)

Table 7
RMSE [mm] in Case 1 and 2.

	Case 1	Case 2	Total
Original	83.77	125.12	105.03
Corrected by TRIM	6.60	12.63	9.94
Corrected by GIM	82.91	122.77	103.33

its formation and still can be mitigated to some degree (see also TRIM ΔTEC in Tables 3 and 5). This is evidenced by comparing Table 10 with uncorrected or GIM-corrected statistics in Case 1 of Table 7. In summary, TRIM map representing the "mean" condition during SAR acquisition correction is still trustworthy to remove first-order ionosphere background mostly in azimuth displacement. This

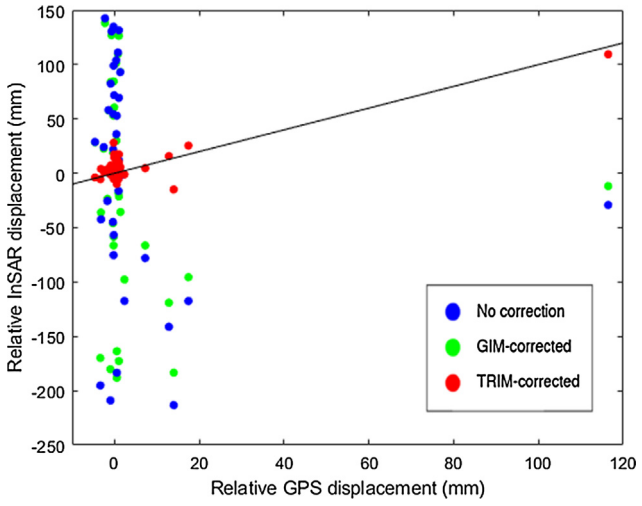

Fig. 6. A scatter plot combining both Case 1 and 2 shows the improved InSAR displacements as compared with GNSS stations, where red dots are TRIM corrected-displacements, green dots are GIM corrected-displacements, and blue dots are uncorrected-displacements. A 1:1 line in black is given for reference. (For interpretation of the references to color in this figure legend, the reader is referred to the web version of this article.)

method is not able to deal with higher order plasma instabilities that cause scintillation and other local effects. A very strong non-constant gradient of ionosphere will induce the non-constant discontinuity in a burst (Liang et al., 2019). It is also a challenging task for most of existing methods.

5.5. Different assumptions of ionosphere shell layer height

In both GIM and TRIM maps, an assumption of the peak ion density is located in 450 km, a fixed height usually seen in the field of global/regional ionospheric maps (Xiang and Gao, 2019). In contrast, our assumption (350 km) located in the middle of varying F2 layer in 250–450 km (Wyatt and Tooley, 2013) is also commonly seen in the literature (Chuo, 2012; Liu et al., 2016; Gomba et al., 2017) and for the wide area augmentation system (Birch et al., 2002). Since the height is related to the projection from STEC to VTEC while using a mapping function, an addition test about the shift of penetration height, and in consequence the shift of penetration window mainly in longitudinal direction, is conducted.

In Table 11, LOS displacement accuracy between 350 km or 450 km assumption is mostly the same for GIM and TRIM. In Case 1 of TRIM, a shift of penetration window to 450 km degrades the accuracy by 1.49 mm. In contrary, TRIM's performance in Case 2 slightly improves by 1.31 mm while using 450 km height. It is concluded that the shell layer height uncertainty will affect the performance of correction. However, the order of difference is relatively small as compared with the improvement from uncorrected results.

6. Conclusion and outlook

In this study, we discuss land displacement over the mid to south Taiwan as retrieved by Sentinel-1 interferograms

Table 8
Differences for large gradient and small gradient in ΔTEC map.

Images Time	ΔTEC in penetration window at 350 km	N-S TEC difference	Ionospheric phase
Master: 2016/01/09 Slave: 2016/02/02	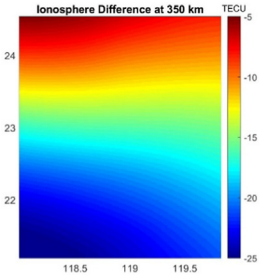	16.73	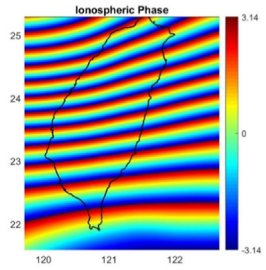
Master: 2016/11/04 Slave: 2016/11/16	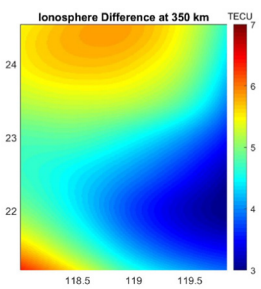	1.19	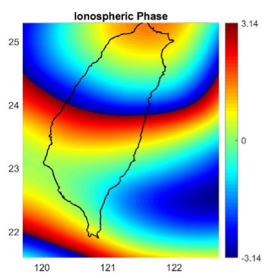

Table 9
Comparison of ionosphere correction with various magnitude of ΔTEC in North-South direction.

Date and North–South TEC Difference	Original Interferogram	TRIM-corrected Interferogram
Master: 2016/05/08 Slave: 2016/05/20 N–S Diff: 12.64 TECU	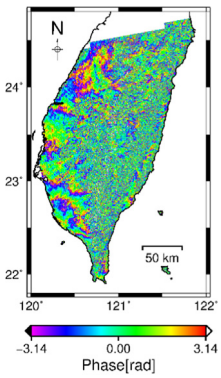	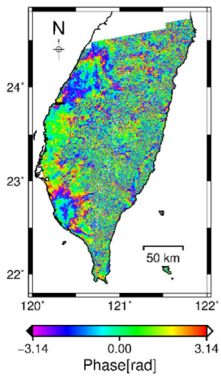
Master: 2016/10/11 Slave: 2016/10/23 N–S Diff: 11.56 TECU	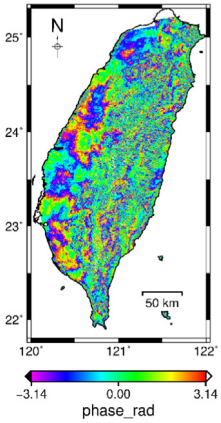	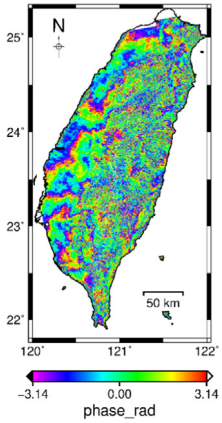
Master: 2016/09/29 Slave: 2016/10/11 N–S Diff: 7.75 TECU	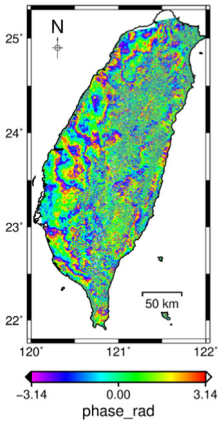	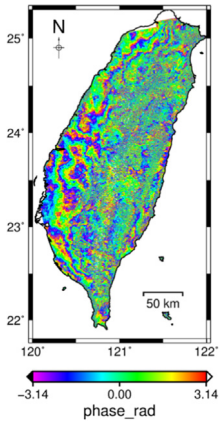
Master: 2016/07/31 Slave: 2016/08/12 N–S Diff: 7.52 TECU	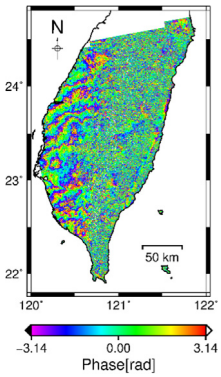	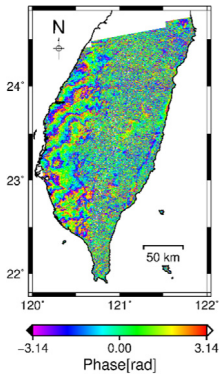

Table 10
Comparison of displacement accuracy as corrected by the neighboring epochs of TRIM TEC map.

Local time of TEC map	09:45	09:50	09:55	10:00	10:05	10:10	10:15
TRIM-corrected accuracy [mm]	34.01	21.36	17.47	6.60	8.90	9.20	10.26

Table 11
LOS displacement accuracy as using different assumptions of penetration height for ionospheric correction. (Unit: mm).

	Case 1	Case 2
Original	83.77	125.12
GIM (350 km/450 km)	82.91/83.67	122.77/106.01
TRIM (350 km/450 km)	6.60/8.09	12.63/11.32

Table A1
TEC characteristics of ascending image pairs.

Pair	Master image	Slave image	Average ΔTEC between images	North to South ΔTEC difference [TECU]	Gradient Rank	Baseline [m]
1	2016/01/09	2016/02/02	16.25	16.73	2	38
2	2016/02/02	2016/02/14	24.26	17.37	1	28
3	2016/02/14	2016/03/09	31.81	2.63		66
4	2016/03/09	2016/03/21	−0.21	−0.80		80
5	2016/03/21	2016/04/14	14.36	0.43		35
6	2016/04/14	2016/05/08	8.93	0.21		29
7	2016/05/08	2016/05/20	13.67	12.64	3	100
8	2016/05/20	2016/06/01	15.47	0.79		76
9	2016/06/01	2016/06/13	11.65	1.46		50
10	2016/07/31	2016/08/12	−1.36	−7.52	6	31
11	2016/08/12	2016/08/24	−11.52	−1.13		66
12	2016/08/24	2016/09/05	6.26	0.32		139
13	2016/09/29	2016/10/11	13.76	7.75	5	50
14	2016/10/11	2016/10/23	28.77	11.56	4	22
15	2016/10/23	2016/11/04	2.29	0.89		28
16	2016/11/04	2016/11/16	4.63	−1.19		53
17	2016/11/16	2016/11/28	−7.21	−1.71		18
18	2016/11/28	2016/12/10	4.55	0.42		29
19	2016/12/10	2016/12/22	3.85	5.20		38
20	2017/01/03	2017/01/15	5.50	2.39		19
21	2017/01/15	2017/01/27	−10.76	−3.33		6
22	2017/01/27	2017/02/08	1.51	0.47		19
23	2017/02/08	2017/02/20	−6.84	−0.47		11
24	2017/02/20	2017/03/04	−2.18	−2.09		48
25	2017/03/04	2017/03/16	6.32	3.39		95
26	2017/03/16	2017/03/28	−1.36	−1.72		49
27	2017/03/28	2017/04/09	−1.42	2.06		75
28	2017/04/09	2017/04/21	−1.03	3.16		15
29	2017/04/21	2017/05/03	−4.35	−6.07		19
30	2017/05/03	2017/05/15	−0.59	0.30		30
31	2017/05/15	2017/05/27	4.22	6.90		131
32	2017/05/27	2017/06/08	1.41	−1.89		87
33	2017/06/08	2017/07/02	6.74	−1.08		33
34	2017/07/02	2017/07/26	−8.67	−2.54		14
35	2017/07/26	2017/08/07	9.21	0.40		4
36	2017/08/07	2017/08/19	−7.34	5.01		30
37	2017/08/19	2017/08/31	−5.86	−5.36		25
38	2017/08/31	2017/09/12	8.73	−2.89		35
39	2017/09/12	2017/09/24	−5.73	−5.52		57
40	2017/09/24	2017/10/06	7.37	2.76		52
41	2017/10/06	2017/10/18	1.29	3.00		15
42	2017/10/18	2017/10/30	−0.13	−4.67		127
43	2017/10/30	2017/11/11	2.04	2.43		59
44	2017/11/11	2017/11/23	3.19	−0.40		47
45	2017/11/23	2017/12/05	−3.32	3.92		170
46	2017/12/05	2017/12/17	4.43	−0.20		33
47	2017/12/17	2017/12/29	−3.12	−5.00		35

in two frames with three sub-swaths each. Regarding the ionosphere effect in the interferogram, both GIM and TRIM TEC maps are examined for the efficacy of phase correction. TRIM based on regional data has higher temporal and spatial resolution than GIM, and thus the ionospheric contribution can be well modeled when a N–S difference in TEC is greater than 16.73 TECU. The preseismic or coseismic deformation caused by an earthquake is still preserved in the corrected results. We find that the zonal pattern caused by ionosphere is obscured when the N–S difference in TEC descends to 12.64 TECU or lower. Regarding the accuracy of DInSAR displacement as compared against GNSS ground station time series, TRIM performs more consistent with in situ data than raw measurements or corrected by a global TEC map. It lowers the RMSE between DInSAR displacement and GNSS ground measurement from 83.77 mm to 6.60 mm and 125.12 mm to 12.63 mm for a preseismic and a coseismic period, respectively. By utilizing a densified TEC map, one can model long-wavelength ionospheric phase contribution and compensate it in the C-band SAR interferogram successfully.

However, it is worth to mention that during these two years the solar cycle 24 was declining from its maximum in April 2014 with a weak strength as compared with earlier solar cycles (Jiang et al., 2015). This phenomenon can be measured by the Auroral Electrojet (AE), an index of geomagnetic variations in the auroral zone in the northern

Table A2
TEC characteristics of descending image pairs.

Pair	Master image	Slave image	Average ΔTEC between images	North to South ΔTEC difference [TECU]	Gradient Rank	Baseline [m]
1	2016/02/16	2016/02/28	14.22	10.32	1	26
2	2016/02/28	2016/03/23	1.85	−5.75	6	36
3	2016/05/10	2016/06/03	2.05	−5.94	4	45
4	2017/08/21	2017/09/02	2.14	−7.23	3	32
5	2017/10/08	2017/10/20	2.81	5.84	5	5
6	2017/10/08	2017/10/20	4.51	9.94	2	14

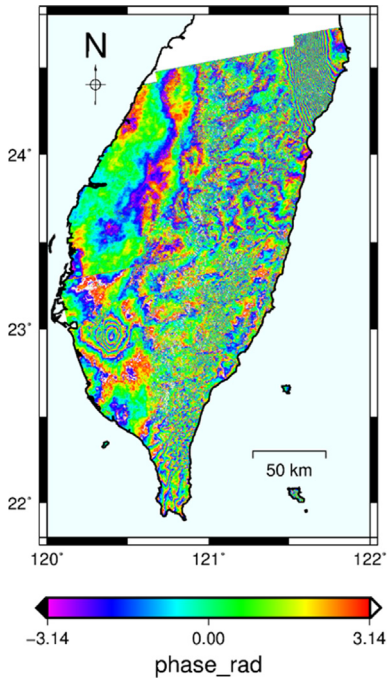

Fig. B1. Split-spectrum solution similar to Gomba et al. (2017) as processed by GMTSAR v5.7. The RMSE achieves 19.86 mm as compared with GNSS stations.

hemisphere, and the Disturbance Storm Time (DsT) that measures the strength of the ring current around Earth caused by solar protons and electrons. Two datasets are available from the World Data Center for Geomagnetism (2015), Kyoto University. As shown in Fig. C1(a)–(b) of Appendix C, AE has relative lower value at the timing of Sentinel-1 images used in this study (red dashed lines in Fig. C1(b)). Similarly, DsT has also lower magnitude in 2016–2017 in Fig. C1(c)–(d). Therefore, the presence of ionospheric contamination on the scale of several hundreds of kilometers are only 2 out of 47 image pairs. In addition, it should be emphasized again that the correction method deploying external TEC map is unable to remove some local effects caused by small plasma activities, due primarily to the scattered samplings from GNSS-based TEC map. An integration with azimuth pixel shifts will be our future work to reduce ionospheric impact on different levels.

Declaration of Competing Interest

The authors declare that they have no known competing financial interests or personal relationships that could have appeared to influence the work reported in this paper.

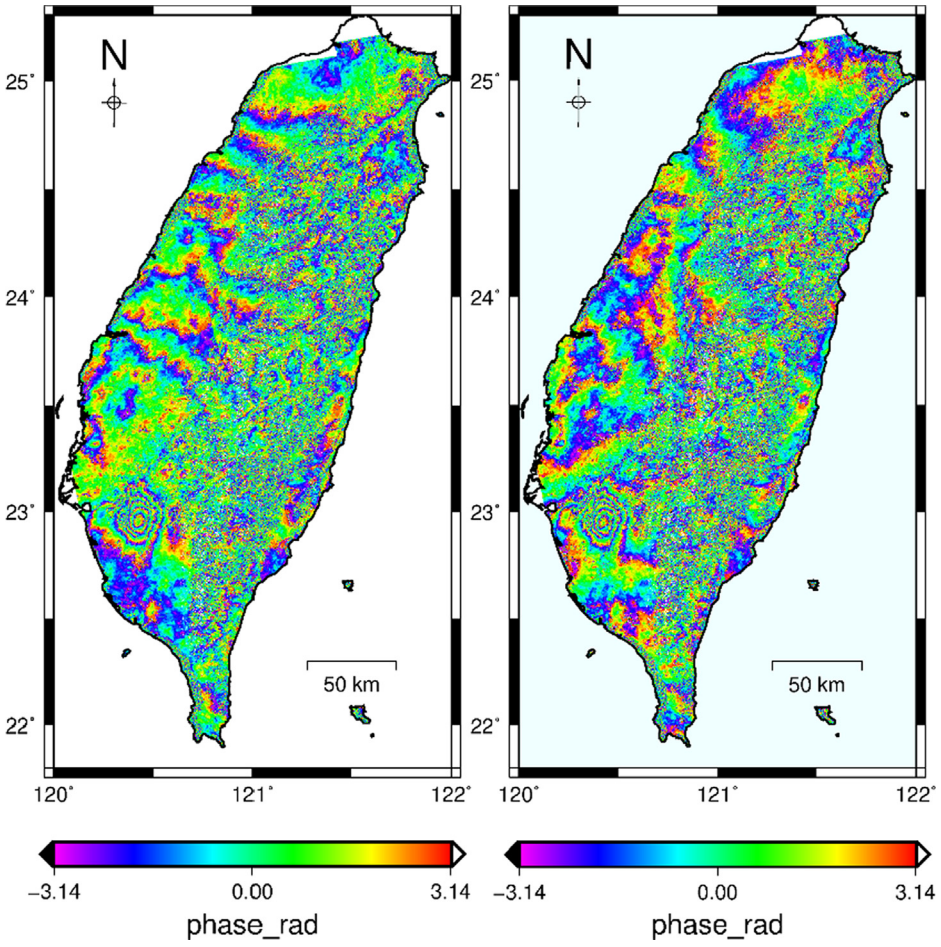

Fig. B2. A test of TRIM correction for the coseismic signal between 2016/02/02 and 2016/03/09. The N–S ΔTEC is 16.1 TECU and the accuracy LOS displacement improves from 46.65 mm (left, before correction) to 43.16 mm (right, after correction) as validated with GNSS stations.

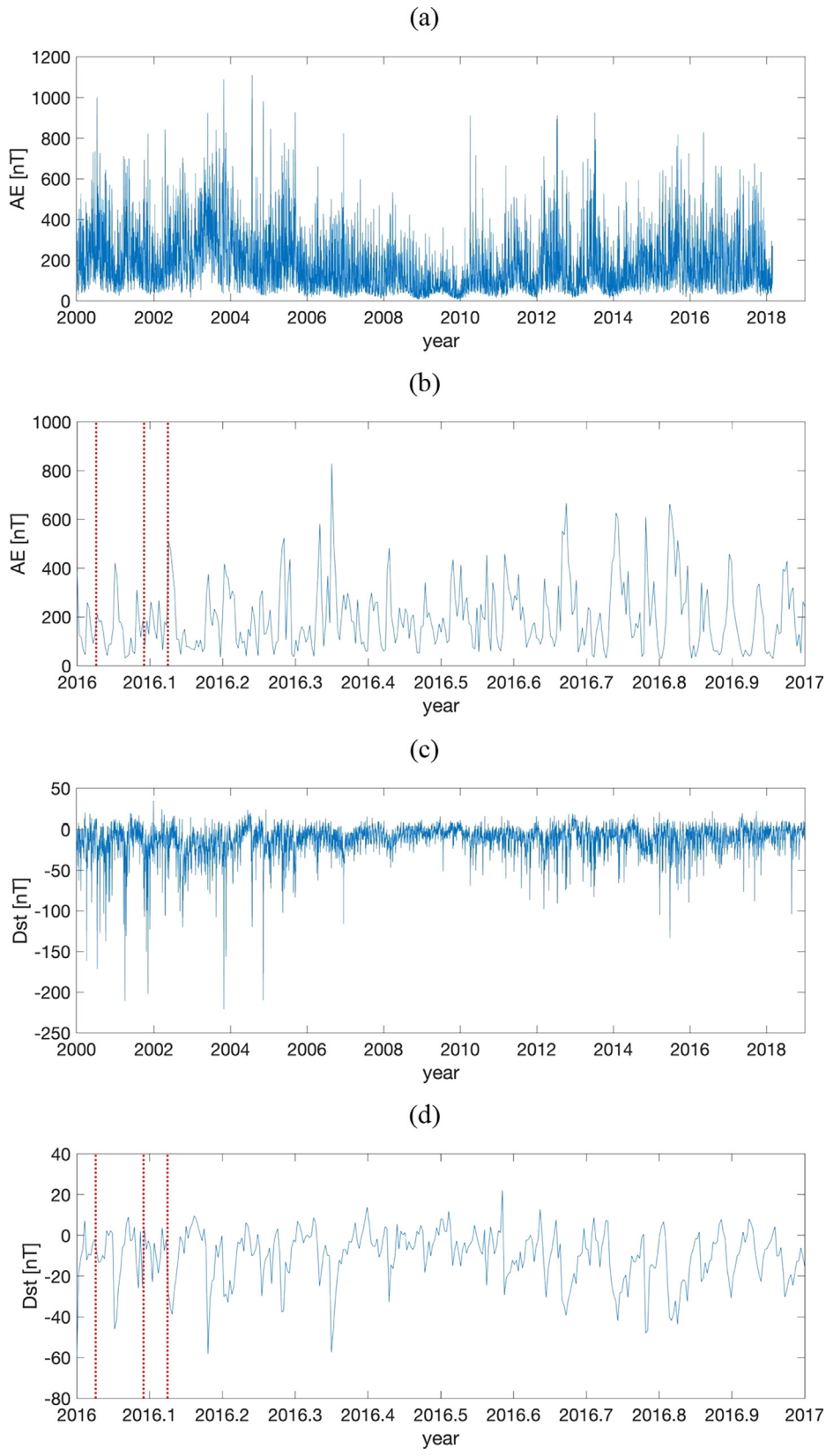

Fig. C1. (a)–(b) Daily solution of AE index in 2000–2018 and 2016–2017. (c)–(d) Daily solution of DsT index in 2000–2018 and 2016–2017. Three red dash lines represent image time of this study. (For interpretation of the references to color in this figure legend, the reader is referred to the web version of this article.)

Acknowledgement

This work was supported in part by the Ministry of Science and Technology (MOST), Taiwan under project number 107-2119-M-008-021, 108-2911-I-008-507, 108-2621-M-008-001, and in part, by the National Central University New Faculty Research Award. We thank ESA, CWB (Taiwan), and World Data Center for Geomagnetism, Kyoto University for providing data used in this study. We thank three anonymous reviewers who provide constructive comments and suggestions.

Appendix A.

See Tables A1 and A2.

Appendix B.

See Figs. B1 and B2.

Appendix C.

See Fig. C1.

References

Birch, M.J., Hargreaves, J.K., Bailey, G.J., 2002. On the use of an effective ionospheric height in electron content measurement by GPS reception. Radio Sci. 37 (1), 1–19.

Bos, A.G., Spakman, W., Nyst, M.C., 2003. Surface deformation and tectonic setting of Taiwan inferred from a GPS velocity field. J. Geophys. Res. Solid Earth 108 (B10).

Brcic, R., Parizzi, A., Eineder, M., Bamler, R., Meyer, F., 2010. Estimation and compensation of ionospheric delay for SAR interferometry. In: 2010 IEEE International Geoscience and Remote Sensing Symposium. IEEE, pp. 2908–2911.

Chen, C.W., Zebker, H.A., 2002. Phase unwrapping for large SAR interferograms: statistical segmentation and generalized network models. IEEE Trans. Geosci. Remote Sens. 40 (8), 1709–1719.

Chuo, Y.J., 2012. Variations of ionospheric profile parameters during solar maximum and comparison with IRI-2007 over Chung-Li, Taiwan. Annales Geophysicae, 30(8), pp. 1249–1257.

Fattahi, H., Simons, M., Agram, P., 2017. InSAR time-series estimation of the ionospheric phase delay: an extension of the split range-spectrum technique. IEEE Trans. Geosci. Remote Sens. 55 (10), 5984–5996.

Feng, J., Zhen, W., Wu, Z., 2017. Ionospheric effects on repeat-pass SAR interferometry. Adv. Space Res. 60 (7), 1504–1515.

Gilman, M., Smith, E., Tsynkov, S., 2013. Reduction of ionospheric distortions for spaceborne synthetic aperture radar with the help of image registration. Inverse Prob. 29 (5), 054005.

Gomba, G., Parizzi, A., De Zan, F., Eineder, M., Bamler, R., 2016. Toward operational compensation of ionospheric effects in SAR interferograms: the split-spectrum method. IEEE Trans. Geosci. Remote Sens. 54 (3), 1446–1461.

Gomba, G., González, F.R., De Zan, F., 2017. Ionospheric phase screen compensation for the Sentinel-1 TOPS and ALOS-2 ScanSAR modes. IEEE Trans. Geosci. Remote Sens. 55 (1), 223–235.

González, P.J., Bagnardi, M., Hooper, A.J., Larsen, Y., Marinkovic, P., Samsonov, S.V., Wright, T.J., 2015. The 2014–2015 eruption of Fogo volcano: Geodetic modeling of Sentinel-1 TOPS interferometry. Geophys. Res. Lett. 42 (21), 9239–9246.

Helmstetter, A., Shaw, B.E., 2009. Afterslip and aftershocks in the rate-and-state friction law. J. Geophys. Res.: Solid Earth 114 (B1). https://doi.org/10.1029/2007JB005077.

Hsieh, C.S., Shih, T.Y., Hu, J.C., Tung, H., Huang, M.H., Angelier, J., 2011. Using differential SAR interferometry to map land subsidence: a case study in the Pingtung Plain of SW Taiwan. Nat. Hazards 58 (3), 1311–1332.

Hsu, Y.J., Simons, M., Avouac, J.P., Galetzka, J., Sieh, K., Chlieh, M., Natawidjaja, D., Prawirodirdjo, L., Bock, Y., 2006. Frictional afterslip following the 2005 Nias-Simeulue earthquake, Sumatra. Science (New York, N.Y.) 312 (5782), 1921–1926.

Huang, M.H., Tung, H., Fielding, E.J., Huang, H.H., Liang, C., Huang, C., Hu, J.C., 2016. Multiple fault slip triggered above the 2016 Mw 6.4 MeiNong earthquake in Taiwan. Geophys. Res. Lett. 43 (14), 7459–7467.

Huang, L., Zhang, H., Xu, P., Geng, J., Wang, C., Liu, J., 2017. Kriging with unknown variance components for regional ionospheric reconstruction. Sensors 17 (3), 468.

Hung, W.C., Hwang, C., Chang, C.P., Yen, J.Y., Liu, C.H., Yang, W.H., 2010. Monitoring severe aquifer-system compaction and land subsidence in Taiwan using multiple sensors: Yunlin, the southern Choushui River Alluvial Fan. Environ. Earth Sci. 59 (7), 1535–1548.

Jee, G., Lee, H.B., Kim, Y.H., Chung, J.K., Cho, J., 2010. Assessment of GPS global ionosphere maps (GIM) by comparison between CODE GIM and TOPEX/Jason TEC data: ionospheric perspective. J. Geophys. Res. Space Phys. 115 (A10).

Jiang, J., Cameron, R.H., Schuessler, M., 2015. The cause of the weak solar cycle 24. Astrophys. J. Lett. 808 (1), L28.

Jung, H.S., Lee, D.T., Lu, Z., Won, J.S., 2013. Ionospheric correction of SAR interferograms by multiple-aperture interferometry. IEEE Trans. Geosci. Remote Sens. 51 (5), 3191–3199.

Liang, C., Agram, P., Simons, M., Fielding, E.J., 2019. Ionospheric correction of InSAR time series analysis of C-band sentinel-1 TOPS data. IEEE Trans. Geosci. Remote Sens. 57 (9), 6755–6773.

Liu, J.Y., Chen, C.H., Sun, Y.Y., Chen, C.H., Tsai, H.F., Yen, H.Y., et al., 2016. The vertical propagation of disturbances triggered by seismic waves of the 11 March 2011 M9. 0 Tohoku earthquake over Taiwan. Geophys. Res. Lett. 43 (4), 1759–1765.

Mattar, K.E., Gray, A.L., 2002. Reducing ionospheric electron density errors in satellite radar interferometry applications. Can. J. Remote Sens. 28 (4), 593–600.

Meyer, F., Bamler, R., Jakowski, N., Fritz, T., 2006. The potential of low-frequency SAR systems for mapping ionospheric TEC distributions. IEEE Geosci. Remote Sens. Lett. 3 (4), 560–564.

Pathier, E., Fruneau, B., Deffontaines, B., Angelier, J., Chang, C.P., Yu, S.B., Lee, C.T., 2003. Coseismic displacements of the footwall of the Chelungpu fault caused by the 1999, Taiwan, Chi-Chi earthquake from InSAR and GPS data. Earth Planet. Sci. Lett. 212 (1–2), 73–88.

Rau, J.-Y. et al., 2017. Science Survey of 2016 Meinong, Kaohsiung, Earthquake. Ministry of Science and Technology, Taiwan.

Reigber, C., Xia, Y., Kaufmann, H., Massmann, F.H., Timmen, L., Bodechtel, J., Frei, M., 1997. Impact of precise orbits on SAR interferometry. ERS SAR Interferometry vol. 406, p. 223.

Rosen, P.A., Hensley, S., Chen, C., 2010. Measurement and mitigation of the ionosphere in L-band interferometric SAR data. In: 2010 IEEE Radar Conference. IEEE, pp. 1459–1463.

Sandwell, D., Mellors, R., Tong, X., Wei, M., Wessel, P., 2011. Open radar interferometry software for mapping surface deformation. Eos Trans. AGU 92 (28).

Sandwell, D.T., Xu, X., Mellors, R., Wei, M., Tong, X., Wessel, P., 2016. GMTSAR: An InSAR Processing System Based on Generic Mapping Tools (second ed.), http://topex.ucsd.edu/gmtsar/tar/GMTSAR_2ND_TEX.pdf.

Schaer, S., Beutler, G., Mervart, L., Rothacher, M., Wild, U., 1995. Global and regional ionosphere models using the GPS double difference phase observable. In: Proceedings of the IGS Workshop on Special Topics and New Directions, Potsdam, Germany, May 15–17, 1995, pp. 77–92.

Schaer, S., Beutler, G., Rothacher, M., 1998. Mapping and predicting the ionosphere. In: Proceedings of the IGS AC workshop, Darmstadt, Germany, 9–11 February, pp. 307–318.

Tseng, K.H., Shum, C.K., Yi, Y., Dai, C., Lee, H., Bilitza, D., Schmidt, M., 2010. Regional validation of Jason-2 dual-frequency ionosphere delays. Mar. Geod. 33 (S1), 272–284.

Tung, H., Hu, J.C., 2012. Assessments of serious anthropogenic land subsidence in Yunlin County of central Taiwan from 1996 to 1999 by Persistent Scatterers InSAR. Tectonophysics 578, 126–135.

Wyatt, D., Tooley, M., 2013. Aircraft Communications and Navigation Systems. Routledge.

Xiang, Y., Gao, Y., 2019. An enhanced mapping function with ionospheric varying height. Remote Sens. 11 (12), 1497.

World Data Center for Geomagnetism, Kyoto, Nose, M., Iyemori, T., Sugiura, M., Kamei, T., 2015. Geomagnetic Dst index, doi: https://doi.org/10.17593/14515-74000 (accessed 2019.10.15).

Xu, X., Sandwell, D.T., Tymofyeyeva, E., González-Ortega, A., Tong, X., 2017. Tectonic and anthropogenic deformation at the Cerro Prieto geothermal step-over revealed by Sentinel-1A InSAR. IEEE Trans. Geosci. Remote Sens. 55 (9), 5284–5292.

Yu, C., Li, Z., Penna, N.T., 2018. Interferometric synthetic aperture radar atmospheric correction using a GPS-based iterative tropospheric decomposition model. Remote Sens. Environ. 204, 109–121.

Zhang, Q., Zhao, Q., 2019. Analysis of the data processing strategies of spherical harmonic expansion model on global ionosphere mapping for moderate solar activity. Adv. Space Res. 63 (3), 1214–1226.

Zhu, W., Ding, X.L., Jung, H.S., Zhang, Q., Zhang, B.C., Qu, W., 2016. Investigation of ionospheric effects on SAR Interferometry (InSAR): A case study of Hong Kong. Adv. Space Res. 58 (4), 564–576.

Zhu, W., Zhang, W.T., He, Y.F., Qu, W., 2017. Performance evaluation of azimuth offset method for mitigating the ionospheric effect on SAR interferometry. J. Sens. 2017, 1–10. https://doi.org/10.1155/2017/4587475.